Journal of Cleaner Production 285 (2021) 125430

Contents lists available at ScienceDirect

Journal of Cleaner Production

journal homepage: www.elsevier.com/locate/jclepro

Realization of high-percentage addition of fly ash in the materials for the preparation of geopolymer derived from acid-activated metakaolin

Haozhe Guo [a, b], Peng Yuan [a, b, *], Baifa Zhang [a, b], Qiang Wang [a, b], Liangliang Deng [a, b], Dong Liu [a, b]

[a] CAS Key Laboratory of Mineralogy and Metallogeny/Guangdong Provincial Key Laboratory of Mineral Physics and Materials, Guangzhou Institute of Geochemistry, Institutions of Earth Science, Chinese Academy of Sciences, 511 Kehua Street, Guangzhou, 510640, China
[b] University of Chinese Academy of Sciences, 19 Yuquan Road, Beijing, 100049, China

ARTICLE INFO

Article history:
Received 11 July 2020
Received in revised form
28 November 2020
Accepted 5 December 2020
Available online 8 December 2020

Handling editor. Prof. Jiri Jaromir Klemeš

Keywords:
Fly ash
Geopolymer
Phosphoric acid
Metakaolin

ABSTRACT

This study focuses on using fly ash to prepare phosphoric acid-activated metakaolin geopolymer, in which the replacement of metakaolin by a high percentage (up to 30%) of fly ash was achieved. The effects of the addition of fly ash on the compressive strength of the resulting geopolymer were tested and statistically analyzed, and the related mechanism was explored through using X-ray diffraction, field emission scanning electron microscope, Fourier-transform infrared, and magic angle spinning nuclear magnetic resonance analysis. The results indicated that the compressive strength of geopolymer maintained at a high level even as a high percentage of fly ash was used to replace metakaolin. The key reason is that fly ash cenospheres effectively optimized the acid-activated geopolymerization of metakaolin. On one hand, cenospheres prevented the plate-like metakaolin particles from being bonded by the aluminum phosphate rapidly generating on the particle surface, which promoted the geopolymerization degree of metakaolin. On the other hand, the three-dimensional network of Si—O—Al—O—P became stronger with the increase of the crosslinking degree of Si, Al, and P under the influence of fly ash cenospheres. These findings demonstrate the feasibility of using fly ash as raw materials for the preparation of high strength phosphoric acid-activated geopolymer, which shows potential for the proper disposal and effective recycling of fly ash.

1. Introduction

Effective recycling of large-scale solid wastes is an important part of globally green and sustainable development. Fly ash (FA) is the byproduct obtained from coal-fired electric power plants. Its global production has reached 750 million tonnes in 2015 (Yao et al., 2015), and shows an upward trend mainly caused by the increasing energy demand in developing countries. The official statistics show that more than 130 million tonnes of FA need to be resource disposal in 2018 alone in China (Ministry of Ecology and Environment of the People's Republic of China, 2020). For developed countries, taking the United States as an example, the rate of FA utilization was only 55.5% in 2018 (American Coal Ash Association (ACAA), 2020). Therefore, to appropriate disposal of the residual FA with large quantity is an urgent worldwide challenge and attracts increasing research interest. Traditionally, the FA waste is dumped into ash ponds or surface impoundments, but such a disposal method inevitably causes a variety of environmental problems such as groundwater contamination and air pollution. For example, since FA normally contains harmful trace elements, such as arsenic (As), chromium (Cr), and lead (Pb) (Gollakota et al., 2019; Koukouzas et al., 2007), the improper disposal of FA bring a big threat of heavy metal pollution to the living environment of human. Despite that, FA possesses some desirable properties (e.g., pozzolanic activity) that allow its utilization in some fields including soil amelioration (Pandey and Singh, 2010), preparation of cement (Hemalatha and Ramaswamy, 2017; Pei et al., 2018; Turgut and Demir, 2019), ceramic (He et al., 2005),

* Corresponding author. CAS Key Laboratory of Mineralogy and Metallogeny, Guangzhou Institute of Geochemistry, Institutions of Earth Science, Chinese Academy of Sciences, Wushan, Guangzhou, 510640, China.
E-mail address: yuanpeng@gig.ac.cn (P. Yuan).

https://doi.org/10.1016/j.jclepro.2020.125430
0959-6526/

zeolite (Yao et al., 2009) and fiber (Rambau et al.); in catalysis (Shaobin, 2008); and as adsorbents for wastewater treatment (Itskos et al., 2010). Among those fields, the construction industry, especially as the additive of ordinary Portland cement (OPC), consumes the most FA (Transparency Market Research, 2019). However, due to a large amount of CO_2 discharged by the industry of OPC production (Peter et al., 2020), more and more efforts have been taking to look for novel construction materials as the substitute for cement. In this regard, solid industrial waste like FA as raw materials for the preparation of the newly emerging construction materials has also being paid much research attention accordingly.

Using alkali-activated geopolymer (GP) for the disposal of FA provides an alternative pathway for achieving the recycling of solid waste and cleaner production (Ferraro et al., 2020; Zhuang et al., 2016). GP is an environment-friendly cementitious material developed by Davidovits in the 1970s, and the materials were firstly named as "geopolymer" in 1979 and gradually accepted by the materials community (Davidovits, 1979, 1991). Low CO_2 emission in the production of GP makes it an ideal substitute for OPC (Alrefaei et al., 2019; Provis and Bernal, 2014). GP produced under the activation of alkali or acid from amorphous aluminosilicate through four processes, namely, depolymerization, diffusion, polycondensation, and solidification (Davidovits, 1989; Khale and Chaudhary, 2007; Provis and van Deventer, 2009). In an early stage, the raw material for the preparation of GP is limited to calcined clay minerals, in which the calcined kaolinite (metakaolin, MK) is the most frequently used raw material. Wastiels (1994) firstly utilized FA as raw material to prepare alkali-activated GP bricks with desired qualities. Since then, FA gradually becomes a raw material or additive for the preparation of alkali-activated GP due to its low cost and widespread availability (You et al., 2019). However, alkali-activated GP itself has some drawbacks, e.g., low ability to resist fire and high temperature (Buchwald et al., 2007), volume instability (Fu et al., 1997), poor acid resistance (Temuujin et al., 2009), and loss of strength over time (Wardhono et al., 2017). The abovementioned disadvantages severely limit the massive recycling of FA through the preparation of alkali-activated GP.

In this work, phosphoric acid-activated GP was used for the recycling of FA for the first time. Phosphoric acid-activated has potentially better performances than alkali-activated GP in performances including corrosion resistance (Wagh, 2011), thermal stability (Celerier et al., 2018; Liu et al., 2010a), mechanical strength (Dan et al., 2008; Gualtieri et al., 2015; Tchakouté and Rüscher, 2017), insulation (Cui et al., 2011; Douiri et al., 2014; Liu et al., 2010b), and utilization of low activated raw material (Zhang et al., 2020a). These advantages of the phosphoric acid-activated GP result from the incorporation of the phosphorus into the 3D structure of GP (Wang et al., 2019a). Thereby, the acid-activated geopolymer has the potential of being used for the recycling of FA. However, using solid wastes for the preparation of phosphoric acid-activated GP has been rarely reported (Wang et al., 2019b). In the present experimental study, FA and MK were used as raw materials for the preparation of acid-activated GP, and various mass fractions of FA were adopted to investigate the effects of FA on the properties of the resulting acid-activated metakaolin GP as well as to assess the feasibility of using FA as raw materials of the acid-activated GP. The results showed that a high percentage of FA (up to 30 mass%) for the preparation of acid-activated metakaolin GP was achieved, without noticeably sacrificing the excellence of the compressive strength of GP. The relevant mechanism was discussed on the basis of a comprehensive analysis of the transformations in the microstructure and chemical environment of elements.

2. Materials and methods

2.1. Materials

Fly ash (FA) was supplied by Foshan Hengyi Thermal Power Plant in Guangdong province, China. Kaolinite was sourced from Maoming, Guangdong province. The chemical compositions of the FA and kaolinite are presented in Table 1. The FA is classified as Class F (ASTM C618-19, 2019) due to its low content of calcium (Ca) (10.80%). Metakaolin (MK) was obtained by calcining kaolinite at 750 °C for 2 h in a muffle furnace. The D_{50} of the MK particles was 58 μm, and that of the FA was 1 μm. The specific gravity of the MK and FA was 2.30 and 2.36, respectively. Laboratory-grade phosphoric acid solution (85 mass%) was used for acid-activation, and ultra-pure water was used throughout the experiments.

2.2. Preparation of phosphoric acid-activated geopolymer

The solid raw materials for the preparation of GP were mixtures of FA and MK mass fractions of FA into MK. Each group of the solid mixture was blended by a ball mill for 1 h to ensure uniformity. The acid activators were prepared by the phosphoric acid and water, which needed to be cooled for 24 h after mixing.

Geopolymers were prepared by adding solid raw materials into the acidic activators. The mixture of solid and liquid was stirred by a cement mixer. Following a low speed stirring for 120 s, a 15 s pause was to scrape the paste on the blade into the mixing pot, and then stirred at a high speed until the past became watery, which meant water formed by dehydrated polycondensation. The resulting paste was cast into the polytetrafluoroethylene (PTFE) molds ($20 \times 20 \times 20$ mm^3), which were then vibrated for 1 min to remove the air bubbles. The molds were covered with plastic film to prevent water loss. The specimens were cured at a temperature of 40 °C and relative humidity of 90%. After 6 days, they were transferred to an oven at 80 °C for 24 h without film. Then the specimens aged at room temperature for further analysis. The final cubic specimens were designated as $G_{5\%FA}$, $G_{10\%FA}$, $G_{20\%FA}$, $G_{30\%FA}$, and $G_{50\%FA}$ according to the mass fractions of FA in the raw materials. Meanwhile, pure MK based GP (denoted G_{MK}) was prepared for comparison. All the samples were synthesized by fixing the molar ratio of Al/P to 1 (Celerier et al., 2018; Gualtieri et al., 2015). An appropriate amount of water was added to the phosphoric acid to make similar fluidity of the different group pastes. Details of the synthetic parameters are shown in Table 2.

2.3. Characterization methods

The chemical compositions were determined by X-ray fluorescence spectrometry (XRF) using a wavelength-dispersive sequential scanning spectrometer (Shimadzu XRF-1800). The particle size distribution and specific surface area were measured by JL-1177 laser particle size analyzer.

The effect of different FA proportions on the mechanical properties of acid-activated GP was characterized by testing the 7- and 100-day compressive strength of specimens determined by a YAW-300D Compression Resistance Tester (LiXian, Zhejiang) with a loading rate of 0.5 N/s. A one-way analysis of variance (ANOVA), followed by a Tukey post hoc test ($P < 0.05$) test were used to compare the compressive strength among the geopolymer groups.

The phase changes before and after the geopolymerization were identified by X-ray diffraction (XRD) analysis, which was taken on a Bruker D8 Advance with Cu-Kα radiation at 40 kV and 40 mA. The scanning range was 3°−70° with a scan rate of 3°/min, and the step width was 0.02°.

Secondary electron image (SEI) mode of a field emission

Table 1
Chemical compositions of the fly ash (FA) and kaolinite (mass, %).

Components	SiO_2	Al_2O_3	CaO	Fe_2O_3	K_2O	Na_2O	MgO	TiO_2	Others	LOI
Fly ash	53.63	21.71	10.80	7.96	1.42	1.21	1.17	0.86	0.76	0.33
Kaolinite	32.11	33.05	0.15	0.06	0.76	1.20	0.30	0.01	8.89	23.33

Table 2
The mass fractions of fly ash in the solid raw materials, and the theoretical molar ratios and solid-to-liquid (S/L) mass ratios between the solid raw material and the phosphoric acid activator.

Samples	Fly ash (mass%)	Theoretical molar ratio		S/L
		Al/P	Si/Al	
G_{MK}	0	1	0.83	0.96
$G_{5\%FA}$	5	1	0.87	0.97
$G_{10\%FA}$	10	1	0.91	0.98
$G_{20\%FA}$	20	1	1.01	1.01
$G_{30\%FA}$	30	1	1.11	1.04
$G_{50\%FA}$	50	1	1.34	1.09

scanning electron microscope (FE-SEM, HITACHI SU8010) was used for the characterization of microstructure. The elemental distribution was obtained using energy-dispersive X-ray spectroscopy (EDS).

Fourier-transform infrared spectra (FT-IR) were recorded on a Bruker VERTEX 70 infrared spectrometer. The FT-IR spectra of the samples in the pressed KBr pellets were collected over a range of 400−4000 cm^{-1}.

Magic angle spinning nuclear magnetic resonance (MAS NMR) experiments were performed on Bruker AVWB III 600 spectrometer. The tests of ^{27}Al and ^{31}P MAS NMR were operated at a resonance frequency of 156.4 MHz and 242.9 MHz, respectively. ^{27}Al MAS NMR spectra were recorded using a small-flip angle technique with a spinning rate of 14 kHz. ^{31}P MAS NMR was carried out on a 4 mm HX double-resonance MAS probe at a sample spinning rate of 12 kHz. Referencing to 1 mol/L aqueous $Al(NO_3)_3$ and 85 mass% H_3PO_4, the chemical shifts of ^{27}Al and ^{31}P were determined.

3. Results and discussion

3.1. Compressive strength of different groups of geopolymer

The 7- and 100-day compressive strengths of different acid-activated GP grouping by the mass fraction of FA on 7- and 100-day are displayed in Fig. 1a. The influence of FA content on the compressive strengths was explored through one-way ANOVA ($P < 0.05$; Table S1) and Tukey post hoc test ($P < 0.05$; Table S2.). Statistically significant differences in compressive strengths were found among the GP in different groups. For 7-day compressive strengths, G_{MK}, $G_{30\%FA}$, and $G_{50\%FA}$ differed among each other, but $G_{5\%FA}$, $G_{10\%FA}$, and $G_{20\%FA}$ had no significant difference. Therefore, the influence of adding FA on the 7-day compressive strengths can divide into three stages: (1) the addition of 5−20 mass% FA decreased the 7-day compressive strengths; (2) the 30 mass% of FA increased the 7-day compressive strength up to 115 MPa; (3) the decrease of 7-day compressive strength appeared again as the additive of fly ash reached 50 mass%. For 100-day compressive strengths, the only statistically significant difference was found in $G_{50\%FA}$. Through long-term aging, the GP containing 5−30 mass% FA obtained statistically similar compressive strengths. The long-term compressive strengths of the resulting GP kept at a high level even as the replacement amount of MK by FA was up to 30 mass%.

At the same time, the addition of FA also affected the growth rates and increments of compressive strengths in 7−100 days. As shown in Fig. 1b, comparing with the negative compressive strength growth rates of G_{MK}, the compressive strengths growth rates of $G_{5\%FA}$, $G_{10\%FA}$, $G_{20\%FA}$, and $G_{50\%FA}$ were all over 50% and gradually decreased with the increasing amount of FA. The biggest increment occurred in $G_{10\%FA}$ and was 36 MPa (from 43 MPa to 79 MPa). The changes of compressive strengths of above samples indicate that the addition of FA did not retard but was favor for the development of compressive strength when the GP was aged for 100 days. Notably, the unexpected negative growth of the compressive strengths happened in $G_{30\%FA}$ like G_{MK}. It may be due to the different shrinking percentage and microstructure transformation of the GP products under high curing temperature, which was affected by the mass ratio of FA and MK (Liew et al., 2016; Rovnaní k, 2010; Zhang et al., 2020b; Cai et al., 2020). Despite that, the 100-day compressive strength of G_{MK} and $G_{30\%FA}$ still stayed at a high level (68 and 61 MPa, respectively). Through comparing the strength development of different groups of GP as described above, the long-term effect of using FA to prepare acid-activated GP on compressive strength was proved to be positive.

Different from the previous alkali-activated GP (Duan et al., 2016; Mustafa et al., 2012; Zhang et al., 2014; Zhang et al., 2014) whose strengths were sensitive to the proportion of FA (Table S3.). The acid-activated GP can achieve high accommodation of FA without much mechanical strength sacrificing both after the short curing and long-term aging. In addition, with the appropriate addition of FA (30 mass%), the short-term compressive strength even to be developed.

3.2. Changes of phase composition and chemical environment of the elements (Si, Al, P) in different groups of geopolymer

3.2.1. X-ray diffraction (XRD) analysis

The XRD patterns of MK and FA are shown in Fig. 2a and h. The broad diffractions, characteristic for the amorphous phase, were observed both in the XRD patterns of MK and FA. Besides, quartz and illite impurities were found in MK, and quartz, mullite, anhydrite, and hematite were found in FA. The centers of the broad diffraction for MK and FA are at 22° (2θ) and 26° (2θ), respectively. According to the area of the broad diffraction patterns, the content of the amorphous phase was roughly evaluated (Williams et al., 2011). The smaller area of the broad diffraction pattern in FA indicates the lower content of the amorphous phase in FA than in MK. Combined with the XRF analysis result of low Ca and Al content in FA, the acid-activated reactivity of FA was poorer than MK. Therefore, with the increasing replacement of MK by FA, the reactivity gradually decreased.

After curing for 7 days, different groups of acid-activated GP were characterized by XRD, and the patterns are presented in Fig. 2b−g. There were no new diffraction patterns formed during the geopolymerization. The greatest changes took place in the central position of the broad diffraction. After reacting with phosphoric acid, all the products show broad diffraction from 14° (2θ) to 38° (2θ) with the center at approximately 27° (2θ), which shifted 5° to a high angle, compared with that of MK. This change was consistent with the feature of the acid-based GP in previous studies (Boonchom and Kongtaweelert, 2009; Cui et al., 2010), which

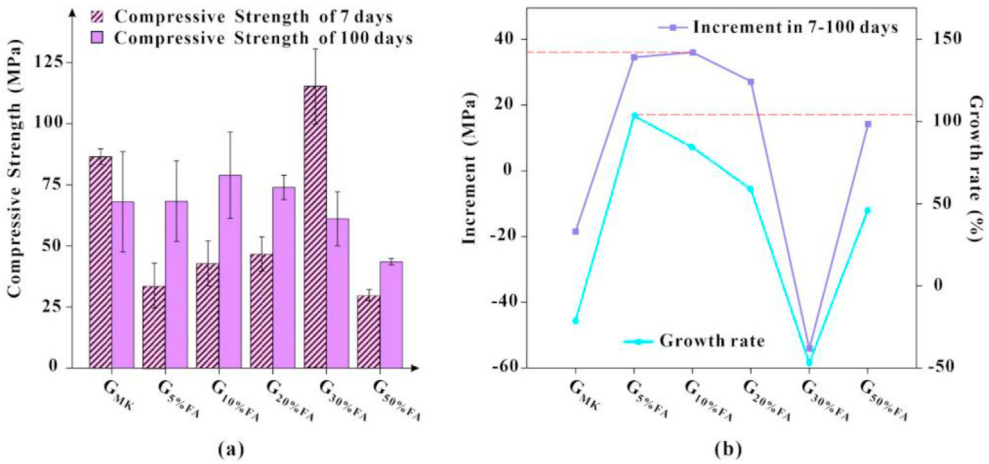

Fig. 1. The 7- and 100-day compressive strengths (MPa) of geopolymer (a) (error bar represents the 95% confidence interval), and the increment and growth rate of compressive strengths (MPa) in 7–100 days (b).

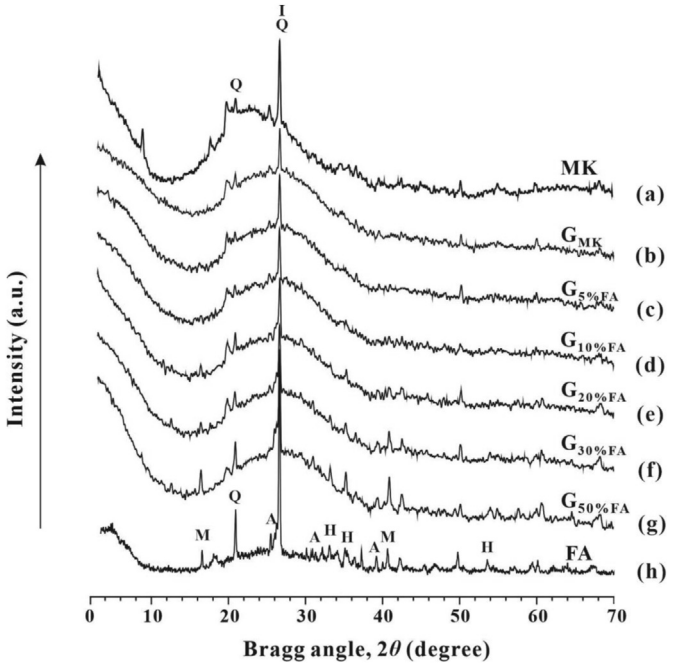

Fig. 2. X-ray diffraction patterns of (a) metakaolin, (b) G_{MK}, (c) $G_{5\%FA}$, (d) $G_{10\%FA}$, (e) $G_{20\%FA}$, (f) $G_{30\%FA}$, (g) $G_{50\%FA}$, and (h) fly ash. (Q: quartz; I: illite; M: mullite; A: anhydrite; H: hematite).

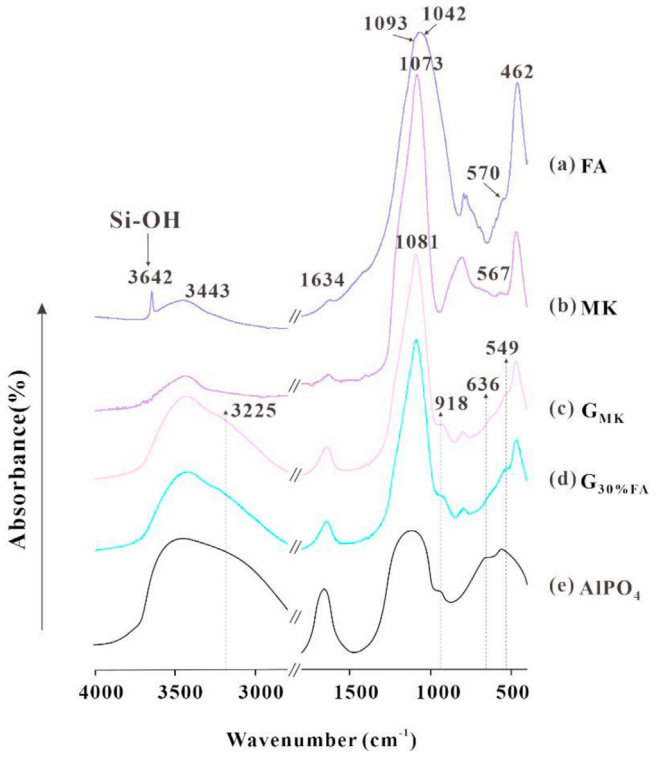

Fig. 3. Fourier-transform infrared spectra of the (a) fly ash, (b) metakaolin, (c) G_{MK}, (d) $G_{30\%FA}$, and (e) aluminum phosphate.

indicates the occurrence of the geopolymerization and the formation of GP in all groups. The areas of the abovementioned broad diffractions of different groups of GP were almost identical, indicating that the amount of the amorphous phase in different GP was almost the same, even 50 mass% of MK was replaced by FA. This phenomenon demonstrates that the acid-activated geopolymerization was not severely affected by the content of FA. Therefore, a high FA addition amount could be achieved in the acid-activated GP without sacrificing much compressive strength.

Notably, the diffraction patterns of the anhydrite in FA and illite in MK disappeared, which indicates that their crystal structures were destroyed under the action of acid-activator and participated in the geopolymerization. The other crystalline phases including quartz, hematite, and mullite in the solid raw materials remained.

3.2.2. Fourier-transform infrared (FT-IR) analysis

Fig. 3a and b displays the FT-IR spectra of FA and MK, and the assignments for the vibrations are reported in Table 3. The strongest band of (Si, Al)–O–Si asymmetric stretching vibration is observed at 1000–1100 cm^{-1}. In the FT-IR spectra of G_{MK} and $G_{30\%FA}$ (Fig. 3c and d), the bands assigned to O–H (3434 and 1640 cm^{-1}) were enhanced compared with raw materials, indicating the increase of the free water in GP. The new appearance bands of 3224 cm^{-1}, 636 cm^{-1}, and 918 cm^{-1}, which were assigned to O–H, P–O–Al, and Al–OH bond (Boonchom and Kongtaweelert, 2009), respectively. This result is consistent with the characteristic bands of aluminum phosphate ($AlPO_4$) (Fig. 3e) (Louati et al., 2016). This

Table 3
Band assignments of the Fourier-transform infrared spectra of the fly ash and metakaolin.

Fly ash		Metakaolin	
Wavenumber (cm^{-1})	Suggested assignments	Wavenumber (cm^{-1})	Suggested assignments
3642	silanol stretching vibration	3434	-OH stretching vibration
3443	-OH stretching vibration	1634	H—O—H bending vibration
1634	H—O—H bending vibration	1073	Si—O—Si(Al) asymmetric stretching vibration
1425	carbonate groups	879	Al—O symmetric stretching vibration
1093 and 1042	Si—O—Si(Al) asymmetric stretching vibration	806	Si—O—Si(Al) symmetric stretching vibration
793 and 776	Doublet of quartz	567	Si—O—Al bending vibration
570	Si—O—Al bending vibration	462	In-plane Si—O bending
462	In-plane Si—O bending		

result demonstrated that the formation of $AlPO_4$ during the geopolymerization. However, it is difficult to directly identify P—O—Al vibration from the strong asymmetric stretching spectra near 1100 cm^{-1}, since the vibration band of P—O—Al and Si—O—Al is overlapping (Sitarz, 2008). Nevertheless, the vibration band of Si—O—Al in raw materials shifted to 1081 cm^{-1} in GP. It is probably related to the formation of the P—O—Al bond. After geopolymerization, the band at approximately 567 cm^{-1} attributed to Si—O—Al bending vibration in the raw materials shifted to 550 cm^{-1}. This confirms that the chemical environment changes in the Si—O—Al bond after geopolymerization. It might be the consequence of the partial replacement of silicon-oxygen tetrahedron ($[SiO_4]$) by phosphorus-oxygen tetrahedron ($[PO_4]$) around Al (Louati et al., 2016), namely the initial Si—O—Al—O—Si bond was transformed into Si—O—Al—O—P. It suggests that one $[AlO_4]$ monomer could react with Si—OH and P—OH at the same time during the geopolymerization.

Moreover, it is worth noting that the discrepancy between G_{MK} and $G_{30\%FA}$ appeared in the bands of 918 cm^{-1} and 550 cm^{-1}. The Al—OH (918 cm^{-1}) vibration band of $G_{30\%FA}$ was weaker and the Si—O—Al (550 cm^{-1}) vibration band was stronger than those of G_{MK}, which is due to that more Al—OH reacted with Si—OH with the addition of 30 mass% FA. The Si—OH in FA which is located at 3642 cm^{-1} may increase the polycondensation of Al and Si by increasing the concentration of Si—OH (Wagh, 2012; Wagh and Jeong, 2010). According to the FT-IR spectra, the main component of GP was identified as amorphous $AlPO_4$ and a small amount of polymerized Si—O—Al—O—P. Due to the addition of FA, more Al—OH reacted with Si—OH which developed the degree of crosslinking in polycondensation.

3.2.3. Magic angle spinning nuclear magnetic resonance (MAS NMR) analysis

The chemical environment of Al and P which were the main chemical components to attend the acid-activated geopolymerization was further confirmed by MAS NMR. The ^{31}P MAS NMR spectra of G_{MK} and $G_{30\%FA}$ are reported in Fig. 4a and b. Both of them exhibit a single resonance peak centered at −15 and −13 ppm, respectively. The position was consistent with the resonance state of $AlPO_4$ (Blackwell and Patton, 1984; Li et al., 2013) which was also evidenced by the FT-IR results. The only one coordination environment of ^{31}P in GP confirmed that P just linked to Al via oxygen, and there was no unreacted $[PO_4]$ monomer due to the lack of peak centered at 0 ppm (Caro et al., 1990; Celerier et al., 2019). It could ensure that phosphoric acid could fully participate in the polycondensation with the Al/P ratio of 1. Although replacing MK by FA caused less activated Al in multicomponent raw materials, there was no appearance of unreacted $[PO_4]$ in $G_{30\%FA}$. The result means that there was still enough Al—OH reacting with P—OH to form GP, which means the amount of GP was not intensely influenced by FA addition.

The ^{27}Al MAS NMR spectra (Fig. 4d and e) exhibits three resonance peaks. The strongest resonance peaks were located at −7 ppm and −6 ppm in G_{MK} and $G_{30\%FA}$, respectively, indicating the main coordination structure of Al in GP was hexa-coordination (Al^{VI}) and its monomer expressed as $[AlO_6]$. Different from the Al^{VI} (6 ppm) in MK (Rocha and Klinowski, 1990), the Al^{VI} in GP shifted toward the low field. It is caused by the $[PO_4]$ linking with the $[AlO_6]$. The P atom is more electronegative than Si, resulting in the chemical shift of the adjacent Al as $[PO_4]$ replaced the $[SiO_4]$ to link with $[AlO_6]$ (Wang et al., 2007). The high compressive strength of products may be related to Al^{VI} which is the most stable in all chemical states of Al. During the polycondensation, the more bridging oxygen the Al had, the greater the degree of crosslinking could be achieved in GP. Thus, Al^{VI} can form a harder 3D network structure than Al^{IV} which was the main coordination structure in traditional alkali-activated GP. A small amount of Al^{VI} located at 6 ppm in both GP was assigned to the unreacted mineral impurities (Wang et al., 2018). Moreover, in GP, the tetra-coordination aluminum (Al^{IV}) also existed. Comparing the chemical shifts of Al^{IV} in G_{MK} and $G_{30\%FA}$ which was located at 47 ppm and 51 ppm, respectively, it was found that the addition of FA caused the shift of Al signal to a higher field. This may be due to the increase of the number of Si connected to Al^{IV}, which coincided with the enhancement of Si—O—Al absorption peak in the FT-IR spectrum. The increased Si—O—Al bonds around Al^{IV} also accelerated the degree of crosslinking, which resulted in a tougher network structure and exhibited high strength of $G_{30\%FA}$ finally.

The results of XRD, FT-IR, and MAS NMR analyses show that $AlPO_4$ was the main component for G_{MK} and $G_{30\%FA}$. It demonstrates that the composition of acid-activated GP was quite different from that of alkali-activated GP. The latter's 3D structure only consists of $[AlO_4]$ and $[SiO_4]$. For acid-activated GP, $[PO_4]$ joined to build the skeleton. Most of the $[PO_4]$ were linked with $[AlO_6]$ which was in the most stable coordination state. The $[AlO_6]$ provided more bridge oxygen atoms to link with the other monomers. The newly-formed $AlPO_4$ is the isostructure of quartz which could exhibit the similar mechanical property of quartz. In addition, when FA replaced 30 mass% of MK, the amount of amorphous GP did not decrease, and more Al—OH reacted with Si—OH, which increased the number of bonds around Al and developed the degree of crosslinking (Fig. 5). It could increase the stability in the 3D network structure and have a positive impact on the performance of compressive strength.

3.3. Effect of material micromorphology on the microstructure of geopolymer

Micromorphology observations of raw materials and GP were achieved by SEM. The MK shows the plate-like structure in the secondary electron image (Fig. 6a). The particles with rounded boundaries stack perpendicular to themselves orderly. The FA in

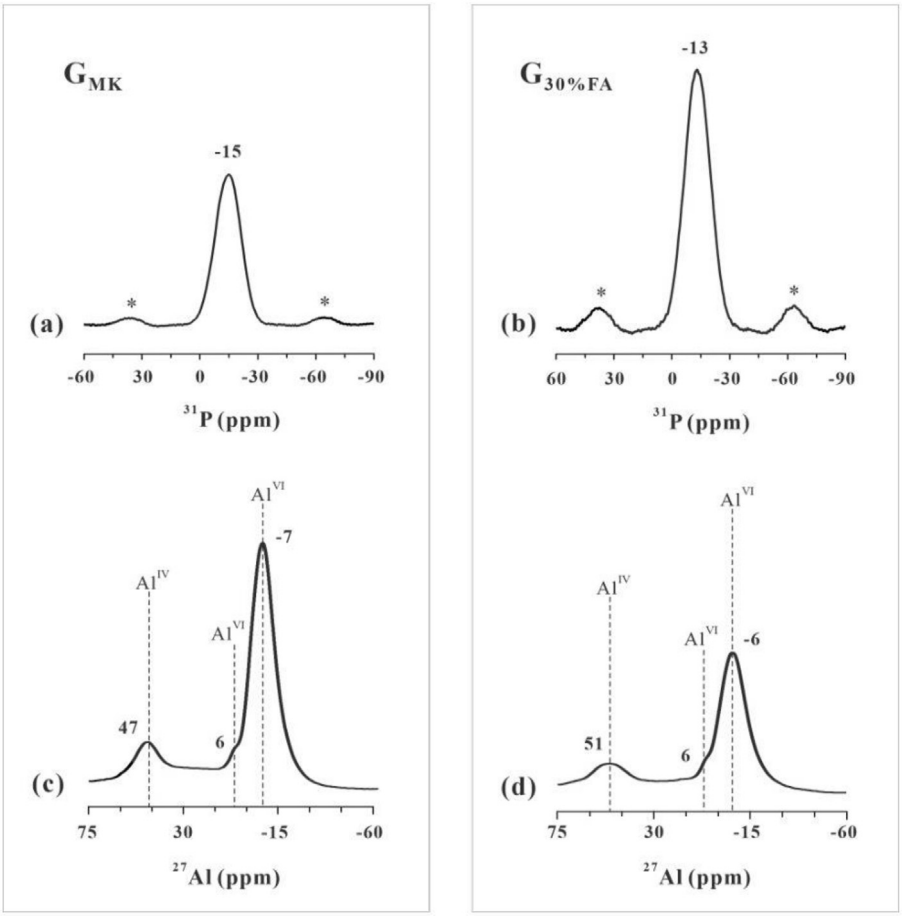

Fig. 4. ^{31}P magic angle spinning nuclear magnetic resonance spectra of (a) G_{MK} and (b) $G_{30\%FA}$; ^{27}Al magic angle spinning nuclear magnetic resonance spectra of (c) G_{MK} and (d) $G_{30\%FA}$. The asterisks denote spinning sidebands.

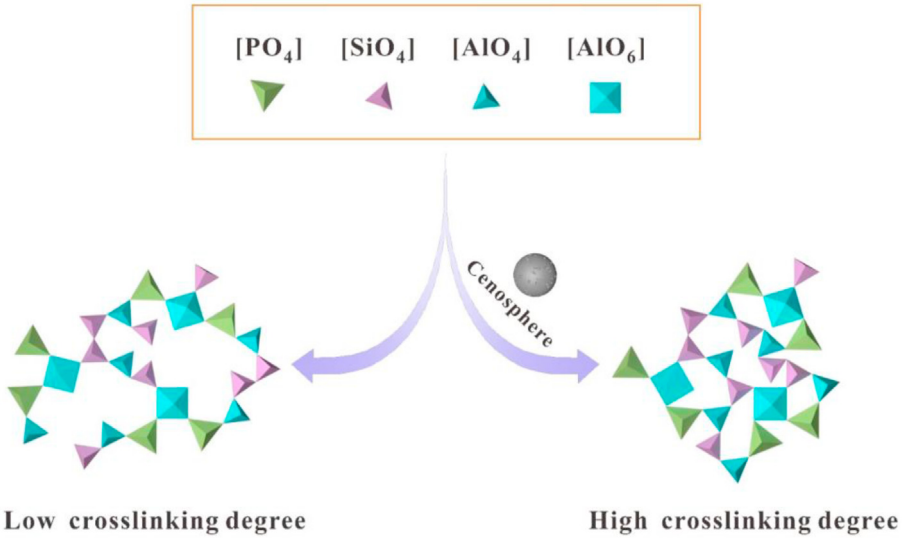

Fig. 5. Schematic diagram of the crosslinking degree influenced by the cenospheres of fly ash.

Fig. 6b is the spherical and irregular shape. The spheres are cenospheres formed by melting and agglomerating of the minerals rich in Si and Al (Yang et al., 2018). EDS spot analysis was used to determine the Si/Al molar ratio of plate-like particles in MK and spherical particles in FA. The average ratio in plate-like particles was 0.83 ± 0.02 (95% confidence interval). While in the sphere particles, the Si/Al molar ratio was varied widely and the composition of each particle is inconsistent. The secondary electron

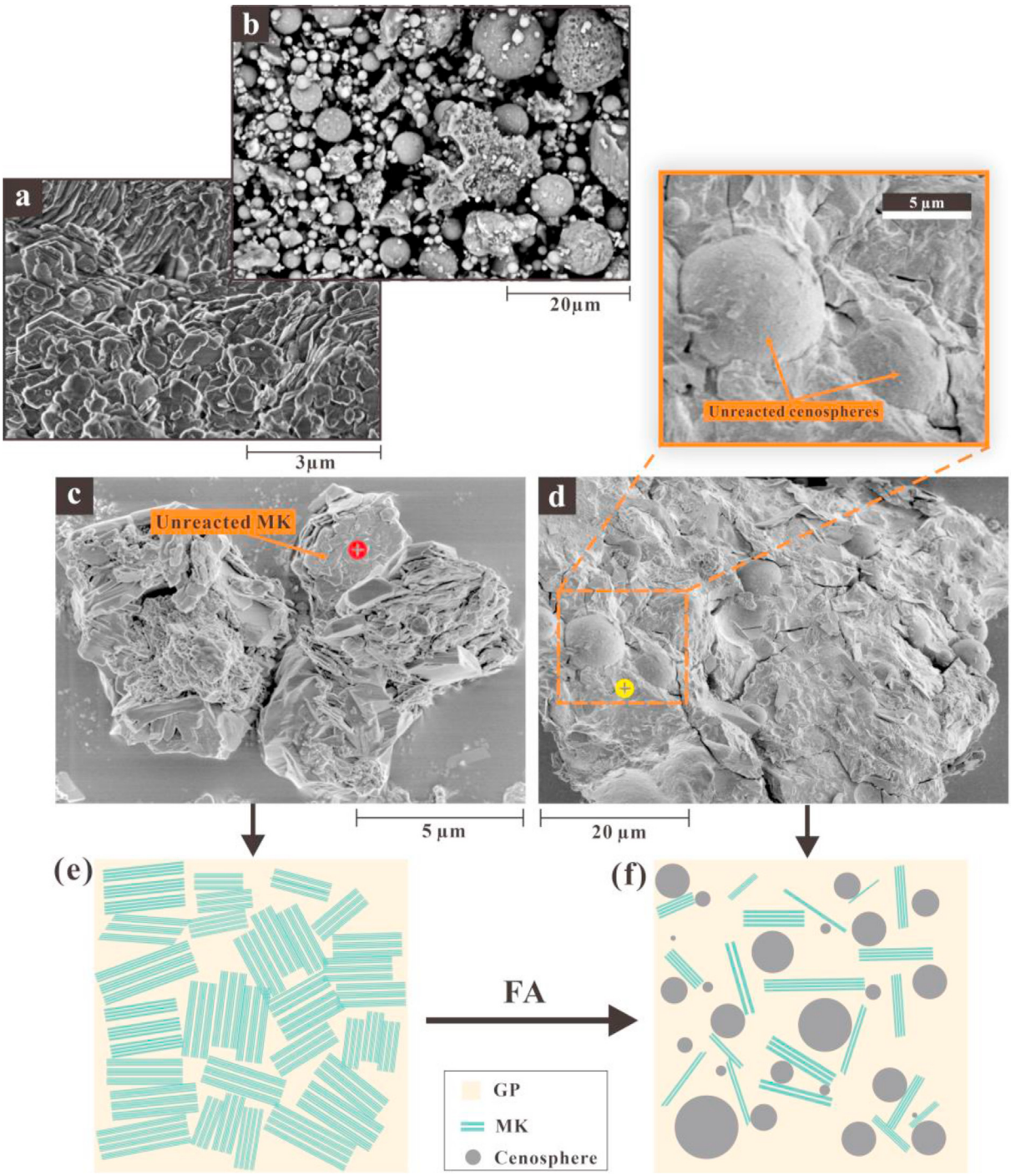

Fig. 6. Secondary electron images of (a) metakaolin, (b) fly ash, (c) G_{MK}, and (d) $G_{30\%FA}$. (e) schematic diagram of stacking plate-like particles bonded by geopolymer. (f) schematic diagram showing the condition of the cenospheres and plate-like metakaolin coexisting. The red spot in (c) represents the sample point of energy-dispersive X-ray spectroscopy spot analysis of plate-like particles in geopolymer and the yellow spot in (d) represents the sample point of energy-dispersive X-ray spectroscopy spot analysis of continuous phase around cenospheres. (For interpretation of the references to color in this figure legend, the reader is referred to the Web version of this article.)

images of the G_{MK} and $G_{30\%FA}$ are given in Fig. 6c and d. The plate-like particles are the unreacted MK. Some of them still stacked orderly, while the others were bonded together by a newly-formed compact phase to form a bigger particle. On the surface of those bonded grains, the cladding phase was also be observed, and it caused the different morphology of the unreacted MK in GP from the initial coarse MK. EDS analysis was performed on these areas (taking the area shown in the red spot). The statistics (Table 4) show that Si/Al increased significantly to 1.30 compared with 0.83 in MK. It demonstrates that large amounts of Al depolymerized under the action of phosphoric acid, and the adjacent Si—O tetrahedral layers of MK remained and interspersed between the unreacted plate-like particles. Meanwhile, the content of P was only 5.12%, which indicates that the formation of the GP phase was just a few. Nevertheless, G_{MK} still shows a superior mechanical strength which reached 75 MPa.

Table 4
The elemental compositions of individual points located in the surrounding of cenospheres and plate-like particles.

		Atom percentage (%)			Molar ratio	
		Si%	Al%	P%	Si/Al	Al/P
Surrounding (yellow spot)	**Mean**	6.49	11.54	13.39	0.56	0.88
	SD	6.82	2.00	2.51	0.61	0.13
Plate-like particles (red spot)	**Mean**	12.80	9.98	5.12	1.30	2.44
	SD	3.87	1.04	2.55	0.16	1.24

In contrast, the unreacted plate-like particles were not observed in $G_{30\%MK}$ (Fig. 6d), which indicates that the MK almost attended the geopolymerization. After adding 30 mass% of FA, there are unreacted cenospheres coated by a compact continuous phase. According to the element content of the continuous phases (taking the area shown in the yellow spot) by EDS spot analysis (shown in Table 4), the average of Al/P molar ratio was 0.88 ± 0.13 which was approximately equal to 1, probably attributing to the formation of $AlPO_4$.

EDS line scan for GP around the cenospheres (Fig. 7a) shows that Al and P were positively correlated and maintained uniform intensity, while they were negatively correlated with Si content. The areas with a high content of Si exhibited spherical and plate-like shape, which were different from the structure of GP and corresponded to the unreacted cenospheres and MK in the secondary electron image, and these unreacted particles were always situated next to the high P and Al areas. This phenomenon is related to the low solubility of silicon oxide in an acidic environment (Fraay, 1990). Thus, during the geopolymerization process, the depolymerization of silicon oxide almost did not occur, but after the depolymerization of aluminum oxide from FA and MK, the residual broken bonds of Si–O in raw material particles could reacted with the H^+ to form Si–OH, which facilitated the polycondensation of Al–OH (Davidovits, 2017).

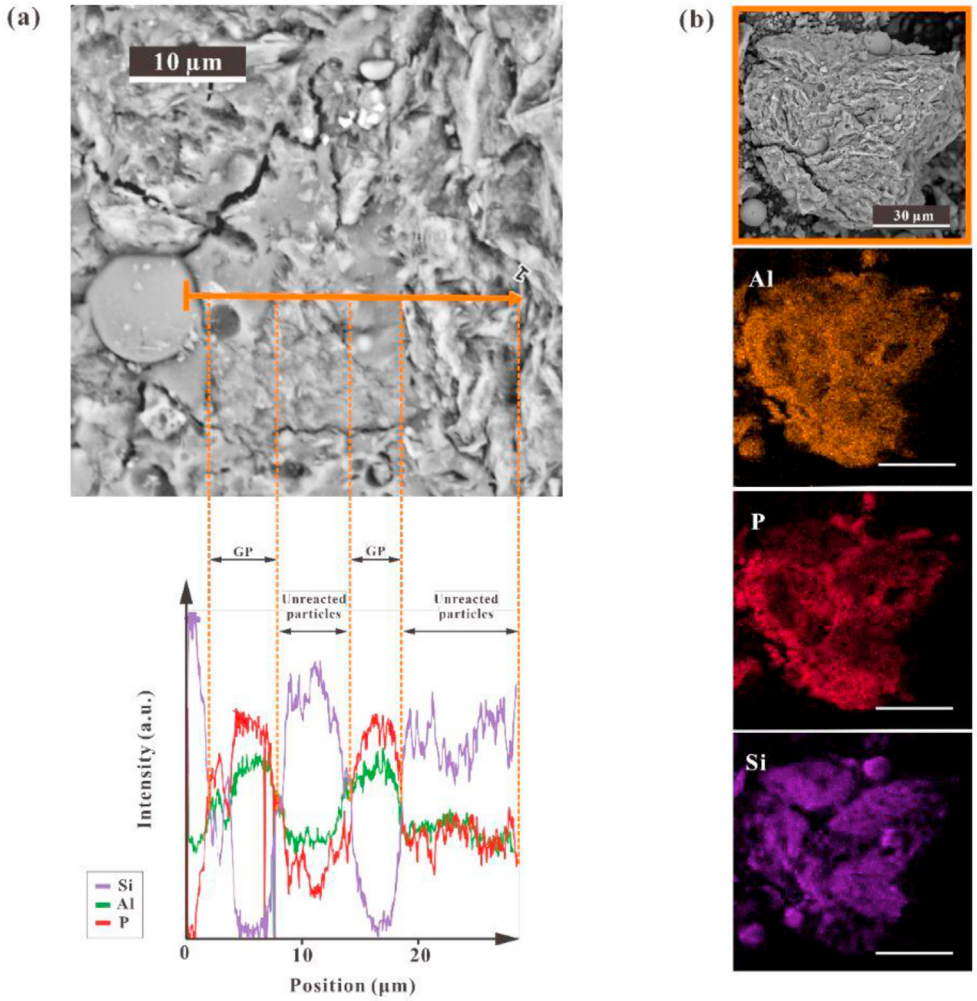

Fig. 7. Microstructures and elemental distributions of $G_{30\%FA}$. (a) secondary electron image of $G_{30\%FA}$ and the orange line showing the location of the energy-dispersive X-ray spectroscopy line scan. The corresponding element contents of Si, P, and Al along the line are shown in the line chart under the secondary electron image. (b) secondary electron image of $G_{30\%FA}$ with corresponding elemental mapping images of Si, P, and Al. (For interpretation of the references to color in this figure legend, the reader is referred to the Web version of this article.)

The EDS element mappings of $G_{30\%FA}$ are shown in Fig. 7b. Same as the line scan, in the element mapping of Si, the region with high Si content matched the position of unreacted cenospheres and MK. In the distribution of P, the color near the surface of the unreacted particles was the brightest, which means that the concentration of P in these areas was higher than those in other areas. This phenomenon reflects that GP was formed on the surface of unreacted particles as well as the line scan analysis. Like the sol-gel reaction, before entering the stage of polycondensation, the formation of monomer in the environment must reach a certain concentration during geopolymerization (Wagh, 2012; Wagh and Jeong, 2010). In the process of depolymerization, [AlO_4] depolymerized from MK diffused to the environment and formed the concentration gradient. From the surface of the particles to the outside, the concentration of [AlO_4] monomer decreased gradually. The concentration of Al monomer near the surface of particles could be the first to reach the requirement to react with [PO_4]. After the forming of GP, unreacted particles were coated and cohered to each other.

In general, the microstructure of GP is like a 'plum pudding'. The unreacted particles are embedded in GP just like plum fixed in the pudding. The GP coats the particles and bonds them together to form a compact structure. However, the difference is that when there is only MK, their bond is directionality due to the two-dimensional shape of the particles, as shown in the schematic diagram (Fig. 6e). The unreacted MK was prone to bond with newly-formed GP to form large particles. Because of the poor mobility of the plate-like structure, the GP between unreacted MK particles is few, which might increase the occurrence of particle fracture. When FA was added, plate-like MK is dispersed under the action of flexible spherical cenospheres, as shown in Fig. 6f. The number of GP around plate-like particles is increasing which is of benefit to the structural fastness.

4. Conclusions

Fly ash and metakaolin were used as raw materials for the preparation of the acid-activated metakaolin geopolymer. The resulting geopolymer showed high compressive strength even as 30 mass% of metakaolin was replaced by the fly ash in the raw materials. The cenospheres of the fly ash were the key factor that strongly affected the acid-activated geopolymerization of metakaolin. Benefiting from the spherical structure of cenospheres, the acid-activated geopolymerization degree of the metakaolin was increased. Cenospheres avoided the plate-like metakaolin being bonded by aluminum phosphate so that increased the amount of metakaolin to depolymerize. In the meantime, the polycondensation between Al—OH and Si—OH was enhanced by the cenospheres of fly ash, which increased the crosslinking degree of Si—O—Al—O—P. As the result, the geopolymer containing fly ash obtained a tougher structure than the metakaolin-based acid-activated geopolymer, which demonstrates the advantage of using fly ash to prepare the acid-activated geopolymer, thus provides a potentially feasible way to achieve the eco-friendly recycling of fly ash.

CRediT authorship contribution statement

Haozhe Guo: Conceptualization, Methodology, Writing - original draft. **Peng Yuan:** Supervision, Conceptualization, Writing - review & editing. **Baifa Zhang:** Investigation. **Qiang Wang:** Resources. **Liangliang Deng:** Writing - review & editing. **Dong Liu:** Writing - review & editing.

Declaration of competing interest

The authors declare that they have no known competing financial interests or personal relationships that could have appeared to influence the work reported in this paper.

Acknowledgments

This work was financially supported by the National Special Support for High-Level Personnel, the National Natural Science Foundation of China (Grant No. 41972045) and the Science and Technology Planning of Guangdong Province, China (Grant Nos. 2017B020237003 and 2020B1212060055). This is a contribution (No. IS-2950) from GIGCAS.

Appendix A. Supplementary data

Supplementary data to this article can be found online at https://doi.org/10.1016/j.jclepro.2020.125430.

References

Alrefaei, Y., Wang, Y.S., Dai, J.G., 2019. The effectiveness of different superplasticizers in ambient cured one-part alkali activated pastes. Cement Concr. Compos. 97, 166—174. https://doi.org/10.1016/j.cemconcomp.2018.12.027.

American Coal Ash Association (ACAA), 2020. ACAA 2018 CCP survey results and production & use charts. https://www.acaa-usa.org/Portals/9/Files/PDFs/2018-Survey-Results.pdf.

ASTM C618-19, 2019. Standard specification for coal fly ash and raw or calcined natural pozzolan for use. Annu. Book ASTM Stand. 3—6. https://doi.org/10.1520/C0618.

Blackwell, C.S., Patton, R.L., 1984. Aluminum-27 and phosphorus-31 nuclear magnetic resonance studies of aluminophosphate molecular sieves. J. Phys. Chem. 88 (25), 6135—6139. https://doi.org/10.1021/j150669a016.

Boonchom, B., Kongtaweelert, S., 2009. Study of kinetics and thermodynamics of the dehydration reaction of $AlPO_4 \bullet H_2O$. J. Therm. Anal. Calorim. 99 (2), 531—538. https://doi.org/10.1007/s10973-009-0113-5.

Buchwald, A., Hilbig, H., Kaps, C., 2007. Alkali-activated metakaolin-slag blends-performance and structure in dependence of their composition. J. Mater. Sci. 42, 3024—3032. https://doi.org/10.1007/s10853-006-0525-6.

Cai, J.M., Li, X.P., Tan, J.W., Vandevyvere, B., 2020. Thermal and compressive behaviors of fly ash and metakaolin-based geopolymer. Journal of Building Engineering 30, 9. https://doi.org/10.1016/j.jobe.2020.101307. Caro, J.

Celerier, H., Jouin, J., Mathivet, V., Tessier-Doyen, N., Rossignol, S., 2018. Composition and properties of phosphoric acid-based geopolymers. J. Non-Cryst. Solids 493, 94—98. https://doi.org/10.1016/j.jnoncrysol.2018.04.044. Cui, X.-m.

Caro, J., Bülow, M., Derewinski, M., Haber, J., Zibrowius, B., 1990. NMR and IR studies of zeolite H-ZSM-5 modified with orthophosphoric acid. J. Catal. 124 (2), 367—375. https://doi.org/10.1016/0021-9517(90)90185-M.

Celerier, H., Jouin, J., Gharzouni, A., Mathivet, V., Sobrados, I., Tessier-Doyen, N., Rossignol, S., 2019. Relation between working properties and structural properties from 27Al, 29Si and 31P NMR and XRD of acid-based geopolymers from 25 to 1000°C. Mater. Chem. Phys. 228, 293—302. https://doi.org/10.1016/j.matchemphys.2019.02.049.

Cui, X.-m., Liu, L.-p., He, Y., Chen, J.-y., Zhou, J., 2011. A novel aluminosilicate geopolymer material with low dielectric loss. Mater. Chem. Phys. 130 (1—2), 1—4. https://doi.org/10.1016/j.matchemphys.2011.06.039.

Cui, X.-m., Liu, L.-p., Zheng, G.-j., Wang, R.-p., Lu, J.-p., 2010. Characterization of chemosynthetic Al2O3—2SiO2 geopolymers. J. Non-Cryst. Solids 356 (2), 72—76. https://doi.org/10.1016/j.jnoncrysol.2009.10.008.

Dan, S.P., Hanna, J.V., Davis, J., Blackford, M.G., Latella, B.A., Sasaki, Y., Vance, E.R., 2008. Relative strengths of phosphoric acid-reacted and alkali-reacted metakaolin materials. J. Mater. Sci. 43 (19), 6562—6566. https://doi.org/10.1007/s10853-008-2913-6.

Davidovits, J., 1979. SYNTHESIS OF NEW HIGH-TEMPERATURE GEO-POLYMERS FOR REINFORCED PLASTICS/COMPOSITES. SPE PACIEC', vol. 79. Society of Plastic Engineers, Brookfield Center, pp. 151—174.

Davidovits, J., 1989. Geopolymers and geopolymeric materials. J. Therm. Anal. 35 (2), 429—441. https://doi.org/10.1007/BF01904446.

Davidovits, J., 1991. Geopolymers: inorganic polymeric new materials. J. Therm. Anal. Calorim. 37 (8), 1633—1656. https://doi.org/10.1007/BF01912193.

Davidovits, J., 2017. Geopolymers: ceramic-like inorganic polymers. J. Ceram. Sci. Technol. 8, 335—350. https://doi.org/10.4416/JCST2017-00038.

Douiri, H., Louati, S., Baklouti, S., Arous, M., Fakhfakh, Z., 2014. Structural, thermal and dielectric properties of phosphoric acid-based geopolymers with different amounts of H_3PO_4. Mater. Lett. 116, 9—12. https://doi.org/10.1016/j.matlet.2013.10.075.

Duan, P., Yan, C., Zhou, W., 2016. Influence of partial replacement of fly ash by

metakaolin on mechanical properties and microstructure of fly ash geopolymer paste exposed to sulfate attack. Ceram. Int. 42 (2), 3504–3517. https://doi.org/10.1016/j.ceramint.2015.10.154.
Ferraro, A., Colangelo, F., Farina, I., Race, M., Fabbricino, M., 2020. Cold-bonding process for treatment and reuse of waste materials: technical designs and applications of pelletized products. Crit. Rev. Environ. Sci. Technol. 1–35. https://doi.org/10.1080/10643389.2020.1776052.
Fraay, A.L.A., 1990. Fly Ash as a Pozzolan in Concrete. Ph.D. thesis. Amsterdam, Nederlands.
Fu, Y., Ding, J., Beaudoin, J.J., 1997. Expansion of portland cement mortar due to internal sulfate attack. Cement Concr. Res. 27 (9), 1299–1306. https://doi.org/10.1016/S0008-8846(97)00133-6.
Gollakota, A.R.K., Volli, V., Shu, C.-M., 2019. Progressive utilisation prospects of coal fly ash: a review. Sci. Total Environ. 672 (JUL.1), 951–989. https://doi.org/10.1016/j.scitotenv.2019.03.337.
Gualtieri, M.L., Romagnoli, M., Pollastri, S., Gualtieri, A.F., 2015. Inorganic polymers from laterite using activation with phosphoric acid and alkaline sodium silicate solution: mechanical and microstructural properties. Cement Concr. Res. 67, 259–270. https://doi.org/10.1016/j.cemconres.2014.08.010.
He, Y., Cheng, W., Cai, H., 2005. Characterization of α-cordierite glass-ceramics from fly ash. J. Hazard Mater. 120 (1), 265–269. https://doi.org/10.1016/j.jhazmat.2004.10.028.
Hemalatha, T., Ramaswamy, A., 2017. A review on fly ash characteristics - towards promoting high volume utilization in developing sustainable concrete. J. Clean. Prod. 147, 546–559. https://doi.org/10.1016/j.jclepro.2017.01.114.
Itskos, G., Koukouzas, N., Vasilatos, C., Megremi, I., Moutsatsou, A., 2010. Comparative uptake study of toxic elements from aqueous media by the different particle-size-fractions of fly ash. J. Hazard Mater. 183 (1–3), 787–792. https://doi.org/10.1016/j.jhazmat.2010.07.095.
Khale, D., Chaudhary, R., 2007. Mechanism of geopolymerization and factors influencing its development: a review. J. Mater. Sci. 42 (3), 729–746. https://doi.org/10.1007/s10853-006-0401-4.
Koukouzas, N., Hämäläinen, J., Papanikolaou, D., Tourunen, A., Jäntti, T., 2007. Mineralogical and elemental composition of fly ash from pilot scale fluidised bed combustion of lignite, bituminous coal, wood chips and their blends. Fuel 86 (14), 2186–2193. https://doi.org/10.1016/j.fuel.2007.03.036.
Li, W., Pierre-Louis, A.-M., Kwon, K.D., Kubicki, J.D., Strongin, D.R., Phillips, B.L., 2013. Molecular level investigations of phosphate sorption on corundum (α-Al2O3) by 31P solid state NMR, ATR-FTIR and quantum chemical calculation. Geochem. Cosmochim. Acta 107, 252–266. https://doi.org/10.1016/j.gca.2013.01.007.
Liew, Y.-M., Heah, C.-Y., Mohd Mustafa, A.B., Kamarudin, H., 2016. Structure and properties of clay-based geopolymer cements: a review. Prog. Mater. Sci. 83, 595–629. https://doi.org/10.1016/j.pmatsci.2016.08.002.
Liu, L.P., Cui, X.M., Qiu, S.H., Yu, J.L., Zhang, L., 2010a. Preparation of phosphoric acid-based porous geopolymers. Appl. Clay Sci. 50 (4), 600–603. https://doi.org/10.1016/j.clay.2010.10.004.
Liu, L.P., Cui, X.M., He, Y., Yu, J.L., 2010b. Study on the dielectric properties of phosphoric acid-based geopolymers. Mater. Sci. Forum 663–665, 538–541. https://doi.org/10.4028/www.scientific.net/MSF.663-665.538.
Louati, S., Baklouti, S., Samet, B., 2016. Geopolymers based on phosphoric acid and illito-Kaolinitic clay. Adv. Mater. Sci. Eng. 2016, 1–7. https://doi.org/10.1155/2016/2359759.
Ministry of Ecology and Environment of the People's Republic of China, 2020. 2018 annual report on prevention and control of solid waste in China's large and medium-sized cities. http://www.mee.gov.cn/ywgz/gtfwyhxpgl/gtfw/201912/P020191231360445518365.pdf.
Mustafa, A.M., Bakri, A., Kamarudin, H., Bnhussain, M., Nizar, I.K., Rafiza, A.R., Zarina, Y., 2012. The processing, characterization, and properties of fly ash based geopolymer concrete. Rev. Adv. Mater. Sci. 30 (1), 90–97. https://doi.org/10.1186/1556-276X-7-96.
Pandey, V.C., Singh, N., 2010. Impact of fly ash incorporation in soil systems. Agric. Ecosyst. Environ. 136 (1), 16–27. https://doi.org/10.1016/j.agee.2009.11.013.
Pei, S.-L., Pan, S.-Y., Gao, X., Fang, Y.-K., Chiang, P.-C., 2018. Efficacy of carbonated petroleum coke fly ash as supplementary cementitious materials in cement mortars. J. Clean. Prod. 180, 689–697. https://doi.org/10.1016/j.jclepro.2018.01.055.
Peter, L., Tiffany, V., Hana, M., Alexandre, G., 2020. https://www.iea.org/reports/cement.
Provis, J.L., Bernal, S.A., 2014. Geopolymers and related alkali-activated materials. Annu. Rev. Mater. Res. 44, 299–327. https://doi.org/10.1146/annurev-matsci-070813-113515.
Provis, J.L., van Deventer, J.S.J., 2009. 1 - introduction to geopolymers. In: Provis, J.L., van Deventer, J.S.J. (Eds.), Geopolymers. Woodhead Publishing, pp. 1–11. https://doi.org/10.1533/9781845696382.1.
Rambau, K.M., Musyoka, N.M., Manyala, N., Ren, J., Langmi, H.W., Mathe, M.K., Preparation of carbon nanofibers/tubes using waste tyres pyrolysis oil and coal fly ash derived catalyst. Environ. Lett.. https://doi.org/10.1080/10934529.2018.1474594.
Rocha, J., Klinowski, J., 1990. 29Si and 27Al magic-angle-spinning NMR studies of the thermal transformation of kaolinite. Phys. Chem. Miner. 17 (2), 179–186. https://doi.org/10.1007/BF00199671.
Rovnaník, P., 2010. Effect of curing temperature on the development of hard structure of metakaolin-based geopolymer. Construct. Build. Mater. 24, 1176–1183. https://doi.org/10.1016/j.conbuildmat.2009.12.023.
Shaobin, W., 2008. Application of solid ash based catalysts in heterogeneous catalysis. Environ. Sci. Technol. 42 (19), 7055–7063. https://doi.org/10.1021/es801312m.
Sitarz, M., 2008. The structure of liquation silico-phosphate glasses. J. Mol. Struct. 887 (1–3), 229–236. https://doi.org/10.1016/j.molstruc.2008.02.002.
Tchakouté, H.K., Rüscher, C.H., 2017. Mechanical and microstructural properties of metakaolin-based geopolymer cements from sodium waterglass and phosphoric acid solution as hardeners: a comparative study. Appl. Clay Sci. 140, 81–87. https://doi.org/10.1016/j.clay.2017.02.002.
Temuujin, J., van Riessen, A., Williams, R., 2009. Influence of calcium compounds on the mechanical properties of fly ash geopolymer pastes. J. Hazard Mater. 167 (1–3), 82–88. https://doi.org/10.1016/j.jhazmat.2008.12.121.
Transparency Market Research, 2019. Fly ash Market. https://www.transparencymarketresearch.com/fly-ash-market-2018-2026.html.
Turgut, P., Demir, F., 2019. The influence of disposed fly ash on Ca2+ leaching and physico-mechanical properties of mortars. J. Clean. Prod. 226, 270–281. https://doi.org/10.1016/j.jclepro.2019.04.105.
Wagh, A.S., 2011. Phosphate geopolymers. Ceram. Eng. Sci. Proc. 32 (10), 91–103. https://doi.org/10.1002/9781118095393.ch9.
Wagh, A.S., 2012. Chemically Bonded Phosphate Ceramics-A Novel Class of Geopolymers. Wiley-Blackwell. https://doi.org/10.1002/9781118408353.ch10.
Wagh, A.S., Jeong, S.Y., 2010. Chemically bonded phosphate ceramics: I, A dissolution model of formation. J. Am. Ceram. Soc. 86 (11), 1838–1844. https://doi.org/10.1111/j.1151-2916.2003.tb03569.x.
Wang, F., Stamboulis, A., Holland, D., Matsuya, S., Takeuchi, A., 2007. Solid state MAS-NMR and FTIR study of barium containing alumino-silicate glasses. Key Eng. Mater. 361–363, 825–828. https://doi.org/10.4028/www.scientific.net/KEM.361-363.825.
Wang, S., Du, P., Yuan, P., Zhong, X., Liu, Y., Liu, D., Deng, L., 2018. Changes in the structure and porosity of hollow spherical allophane under alkaline conditions. Appl. Clay Sci. 166, 242–249. https://doi.org/10.1016/j.clay.2018.09.028.
Wang, Y.S., Alrefaei, Y., Dai, J.G., 2019a. Silico-Aluminophosphate and alkali-aluminosilicate geopolymers: a comparative review. Front. Mater. 6, 106. https://doi.org/10.3389/fmats.2019.00106.
Wang, Y.S., Alrefaei, Y., Dai, J.G., 2019b. Improvement of early-age properties of silico-aluminophosphate geopolymer using dead burnt magnesia. Construct. Build. Mater. 217, 1–11. https://doi.org/10.1016/j.conbuildmat.2019.05.050.
Wardhono, A., Gunasekara, C., Law, D.W., Setunge, S., 2017. Comparison of long term performance between alkali activated slag and fly ash geopolymer concretes. Construct. Build. Mater. 143, 272–279. https://doi.org/10.1016/j.conbuildmat.2017.03.153.
Wastiels, J., Wu, X., Faignet, S., Patfoort, G., 1994. Mineral polymer based on fly ash. J. Resour. Manag. Technol. 22 (3), 135–141.
Williams, R.P., Hart, R.D., van Riessen, A., 2011. Quantification of the extent of reaction of metakaolin-based geopolymers using X-ray diffraction, scanning electron microscopy, and energy-dispersive spectroscopy. J. Am. Ceram. Soc. 94 (8), 2663–2670. https://doi.org/10.1111/j.1551-2916.2011.04410.x.
Yang, T., Zhu, H., Zhang, Z., 2018. Effect of fly ash microsphere on the rheology and microstructure of alkali-activated fly ash/slag pastes. Cement Concr. Res. 109, 198–207. https://doi.org/10.1016/j.cemconres.2018.04.008.
Yao, Z.T., Xia, M.S., Ye, Y., Zhang, L., 2009. Synthesis of zeolite Li-ABW from fly ash by fusion method. J. Hazard Mater. 170 (2), 639–644. https://doi.org/10.1016/j.jhazmat.2009.05.018.
Yao, Z.T., Ji, X.S., Sarker, P.K., Tang, J.H., Ge, L.Q., Xia, M.S., Xi, Y.Q., 2015. A comprehensive review on the applications of coal fly ash. Earth Sci. Rev. 141 (141), 105–121. https://doi.org/10.1016/j.earscirev.2014.11.016.
You, S., Ho, S.W., Li, T., Maneerung, T., Wang, C.H., 2019. Techno-economic analysis of geopolymer production from the coal fly ash with high iron oxide and calcium oxide contents. J. Hazard Mater. 361, 237–244. https://doi.org/10.1016/j.jhazmat.2018.08.089.
Zhang, H.Y., Kodur, V., Qi, S.L., Cao, L., Wu, B., 2014. Development of metakaolin–fly ash based geopolymers for fire resistance applications. Construct. Build. Mater. 55 (4), 38–45. https://doi.org/10.1016/j.conbuildmat.2014.01.040.
Zhang, Z., Hao, W., Zhu, Y., Reid, A., Provis, J.L., Bullen, F., 2014. Using fly ash to partially substitute metakaolin in geopolymer synthesis. Appl. Clay Sci. 88–89 (3), 194–201. https://doi.org/10.1016/j.clay.2013.12.025.
Zhang, B., Guo, H., Deng, L., Fan, W., Yu, T., Wang, Q., 2020a. Undehydrated kaolinite as materials for the preparation of geopolymer through phosphoric acid-activation. Appl. Clay Sci. 199, 105887. https://doi.org/10.1016/j.clay.2020.105887.
Zhang, B., Yuan, P., Guo, H., Deng, L., Li, Y., Li, L., Wang, Q., Liu, D., 2020b. Effect of curing conditions on the microstructure and mechanical performance of geopolymers derived from nanosized tubular halloysite. Construct. Build. Mater. 121186. https://doi.org/10.1016/j.conbuildmat.2020.121186.
Zhuang, X.Y., Chen, L., Komarneni, S., Zhou, C.H., Tong, D.S., Yang, H.M., Yu, W.H., Wang, H., 2016. Fly ash-based geopolymer: clean production, properties and applications. J. Clean. Prod. 125, 253–267. https://doi.org/10.1016/j.jclepro.2016.03.019.